Structural and electronic properties of rare-earth chromites: A computational and experimental study

Jianhang Shi,[1,2] Gayanath W. Fernando,[3] Yanliu Dang,[2] Steven L. Suib,[2,4] and Menka Jain[2,3,*]
[1]*Department of Materials Science and Engineering, University of Connecticut, Storrs, Connecticut 06269, USA*
[2]*Institute of Materials Science, University of Connecticut, Storrs, Connecticut 06269, USA*
[3]*Department of Physics, University of Connecticut, Storrs, Connecticut 06269, USA*
[4]*Department of Chemistry, University of Connecticut, Storrs, Connecticut 06269, USA*

(Received 25 April 2022; revised 8 July 2022; accepted 28 September 2022; published 18 October 2022)

In this work, the structural, optical, and electronic properties of rare-earth perovskites of the general formula $R\mathrm{CrO}_3$, where R represents the rare-earth Gd, Tb, Dy, Ho, Er, and Tm, have been studied in detail. These compounds were synthesized through a facile citrate route. X-ray diffraction, Raman spectroscopy, and UV-Visible spectroscopy were utilized to reveal the structural evolutions in $R\mathrm{CrO}_3$. The lattice parameters, Cr^{3+}–O^{2}–Cr^{3+} bond angle, and CrO_6 octahedral distortions were found to strongly depend on the ionic radii of R. First-principles calculations based on density-functional theory within the generalized gradient approximation (GGA) of Perdew-Burke-Ernzerhof (PBE) and strongly constrained and appropriately normed (SCAN) meta-GGA were also employed to calculate the structural and electronic properties of $R\mathrm{CrO}_3$. The ground-state energy, lattice constants, electronic structures, and density of states of $R\mathrm{CrO}_3$ were calculated. These provide some insights into the electronic characteristics of the $R\mathrm{CrO}_3$ compounds. The calculated values of lattice parameters and band gaps with Hubbard U correction (SCAN + U) agree well with values measured experimentally and show more accuracy in predicting the ground-state crystal structure and band structure compared to PBE + U approximation. The band gap of $R\mathrm{CrO}_3$ is found to be independent of the ionic radii of R from both experiments and calculations.

DOI: 10.1103/PhysRevB.106.165117

I. INTRODUCTION

Oxides consisting of rare-earth element (R) with partially occupied $4f$ shell are crucial in modern technologies due to their various intriguing magnetic, luminescent, and electrochemical properties for potential applications as multifunctional materials [1,2]. Investigations on oxides, such as rare-earth orthoferrites ($R\mathrm{FeO}_3$) [3–5], manganites ($R\mathrm{MnO}_3$) [6–8], nickelates ($R\mathrm{NiO}_3$) [9–11], and orthochromites ($R\mathrm{CrO}_3$) [12–14], have provided remarkable opportunities to enhance our understanding of the relationships between structural and physical properties [15]. Among the rare-earth oxides, the $R\mathrm{CrO}_3$ with a distorted perovskite structure exhibiting unique interesting properties, such as spin reorientation, magnetization reversal, and large magnetocaloric effect, are currently attracting increasing research interest [15]. The $R\mathrm{CrO}_3$ family of materials have shown to exhibit a G-type canted antiferromagnetism below Néel temperature, T_N^{Cr}, where the Cr^{3+} spin orders [16]. The canting is presumed to be the source of weak ferromagnetism, which is the result of antisymmetric Dzyaloshinskii-Moriya interaction [17]. The transition temperatures (T_N^{Cr}) have been reported to shift to higher values with the increasing ionic radii of the R-ion, which could be attributed to the decreasing lattice distortions and increasing Cr^{3+}–O^{2-}–Cr^{3+} bond angles [18]. Recently, some of the rare-earth chromites were reported to be magnetoelectric multiferroics due to the coexistence of the electric and magnetic orders, as in GdCrO_3 [19]. These properties allow $R\mathrm{CrO}_3$ for possible practical applications such as spin-injection devices and nonvolatile magnetic random access memories. For periodic solids, first attention by the computational solid-state community goes towards predicting the fundamental band gap of materials due to its relevance in technological applications, such as optoelectronics and photovoltaics. $R\mathrm{CrO}_3$ materials have also been studied as optically active photocatalyst due to the presence of slightly distorted CrO_6 octahedral complex [17]. Some materials of the $R\mathrm{CrO}_3$ family have been reported to have wide band gap with a value ranging from 2.19 to 3.20 eV based on the results obtained from the UV-Visible (UV-Vis) spectroscopy [17].

Theoretically, first-principles computational techniques based on density-functional theory (DFT) provide an extremely valuable tool for predicting the stable structures and energetics of materials for both finite and periodic systems [20]. Several approximations have been developed to allow for calculations at various levels of accuracy, such as generalized gradient approximation (GGA) in a standard form of Perdew-Burke-Ernzerhof (PBE) and meta-GGA in the form of the strongly constrained and appropriately normed (SCAN) functional [21]. However, these approximations could sometimes dramatically underestimate the band gaps (E_g) for strongly correlated systems or insulators due to the existence of a derivative discontinuity of the energy with respect to the number of electrons or the use of a local potential to represent exchange interactions [22–24]. For rare-earth compounds, the

---

[*] Corresponding author: menka.jain@uconn.edu

f- and d-orbital correlations are also important when and where some atomic character of the orbitals survives, and spin-orbit effects are strong. The local-density approximation (LDA + U) type schemes were developed in the context of Mott-Hubbard insulators and are applicable in cases such as the f-electron systems where the atomic orbital character (as opposed to the itinerant character) survives to an appreciable degree. This is of course an approximate way to deal with strong correlations. In these cases, the accuracy of the DFT approximations is improved by incorporating a Hubbard model–type correction (+U, correction to approximate DFT functionals such as, e.g., LDA, GGA, or meta-GGA), in which an empirical on-site potential (U) is added to the atomic pseudopotential to account for localized d and f orbitals [25]. For many magnetoelectric multiferroic materials, such as $TbMnO_3$, $HoMnO_3$, etc., the first-principles results have been shown to be very sensitive to the choice of the on-site potential [26]. We note that spin-polarized versions of such density functionals have to be implemented when studying magnetic materials.

There are only a few reports on the standard calculations of the RCrO$_3$ based on DFT to understand their band structure. For example, Terkhi *et al.* reported a band gap of 2.15 eV of $GdCrO_3$ calculated by the modified Becke-Johnson exchange potential using the WIEN2K code [27], which is lower than the experimentally observed value of 3.15 eV [17]. Terkhi *et al.* also demonstrated the band gap of $NdCrO_3$ underestimated by GGA-PBE could be more accurately predicted by GGA plus Tran-Blaha modified Becke-Johnson scheme [28]. The band gap for $DyCrO_3$ was calculated to be 2.7 eV where for the exchange and correlation energy, the PBE functional under GGA was employed via the Vienna *Ab initio* Simulation package (VASP), which is also lower than its experimentally observed value of 3.19 eV [17,29]. This band gap of 2.7 eV is attributed to the charge-transfer gap between O 2p and Cr 3d states. In the work by Ong *et al.*, three optical gaps were identified: (i) a charge-transfer gap of 3.40 eV, (ii) a gap of 2.15 eV responsible for its green color, and (iii) an energy band gap of 1.40 eV between the occupied Cr t_{2g} and unoccupied Cr e_g orbitals [30]. However, in case of pure $LaCrO_3$, the band gap of 2.15 eV is not revealed by the reflectivity measurement that would make it a colorless material, which is in contradiction to its observed light-green color. Although the aforementioned efforts have been made, the electronic structures of some RCrO$_3$ compounds are still not well understood from a theoretical point of view. Theoretical work in this direction can lead to the useful insights of the underlying physics of the evolution of their electronic structure and provide crucial information that can lead to the design of materials with enhanced physical properties, such as multiferroic behavior in the RCrO$_3$ family of materials.

In this paper, we report experimental and theoretical investigations of the structural and electronic properties in the RCrO$_3$ family of materials (R = Gd, Tb, Dy, Ho, Er, and Tm) synthesized via a solution route. The experimentally observed optical band gap of ∼3.3 eV is found to be related to the transitions between the O 2p valence band and the bottom of the conduction band. DFT-based calculations are performed within a collinear arrangement of R^{3+} and Cr^{3+} spins, where the two exchange-correlation functionals were used within VASP: (PBE) GGA and (SCAN) meta-GGA functionals. The on-site Coulomb interaction correction was applied to both functionals, which after correction are called PBE + U and SCAN + U methods. This is a systematic experimental and theoretical study of the RCrO$_3$ material for determining relations between the structural modulation and electronic properties.

II. EXPERIMENTAL AND COMPUTATIONAL DETAILS

The bulk powder samples of RCrO$_3$ (R = Gd, Tb, Dy, Ho, Er, and Tm) were synthesized by a citrate solution route. For this, high-purity (>99.99%) nitrate salts were obtained from Alfa Aesar. At first, the metal salts were dissolved in water stoichiometrically and then mixed together with citric acid. The obtained solution was continuously stirred, heated, and dried on a hot plate. The resultant powder was then grinded in mortar pestle and annealed at 900 °C for 2 h in oxygen atmosphere to obtain $GdCrO_3$ (GCO), $TbCrO_3$ (TbCO), $DyCrO_3$ (DCO), $HoCrO_3$ (HCO), $ErCrO_3$ (ECO), and $TmCrO_3$ (TmCO) bulk powder samples. The crystal structure of these powder samples was examined by x-ray diffraction (XRD, Bruker D2 Phaser diffractometer with Cu-Kα radiation) and by Raman spectroscopy (Renishaw System 2000 using 514-nm Ar-ion laser) techniques. The UV-Vis spectra of the samples were recorded using a Shimadzu UV-2450 UV-Vis Spectrometer in a range of 200–800 nm using deuterium and halogens.

DFT-based spin-polarized electronic-structure calculations were carried out using the projector-augmented wave method as implemented in VASP [31,32], with a kinetic energy cutoff of 520 eV and a total energy convergence threshold of 10^{-6} eV [29]. In this work, the exchange-correlation interaction is treated within the GGA using the PBE functional and within the meta-GGA using the SCAN functional, both with on-site Coulomb interactions (PBE + U, SCAN + U) for a better treatment of 3d(Cr^{3+}) and 4f(R^{3+}) electrons [33]. The structural properties and band structure of RCrO$_3$ are investigated here using PBE + U and SCAN + U and the two results are compared. The on-site Coulomb interaction presented in 3d states of the transition-metal ion is corrected by the DFT + U (U is the Hubbard energy) method and the U value was set as 3 eV for Cr 3d states, in line with previous works [20,28]. The Hubbard-U values for Gd, Tb, Dy, Ho, Er, and Tm were taken as 4.6, 5.0, 5.0, 4.9, 4.2, and 4.8 eV, respectively, according to the work by Topsakal *et al.* [34]. We assume a 3+ oxidation state of rare earth ion with 4f electrons either frozen in the ionic core or included as valence electrons. The spin-orbit coupling and noncollinear magnetic states are not considered in these calculations. A $10 \times 10 \times 7$ Γ-centered k-point mesh was used to sample the Brillouin zone corresponding to the 20-atom orthorhombic cell. The structures were fully relaxed until the forces acting on the atoms were smaller than 0.005 eV/Å.

III. RESULTS AND DISCUSSION

A. Spin configuration

Three types of antiferromagnetic (AFM) spin structures are possible for R^{3+}/Cr^{3+} spins: G-AFM, C-AFM, and A-AFM

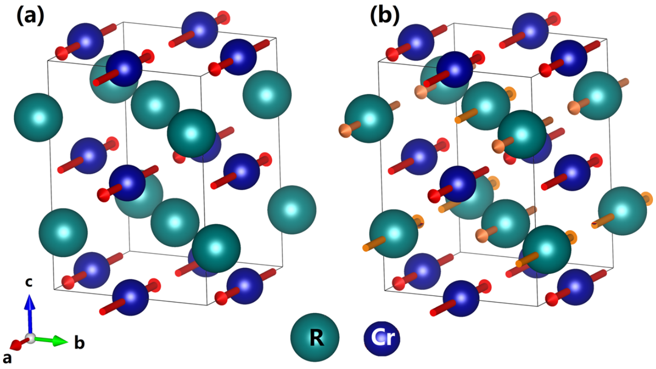

FIG. 1. Spin configurations of R^{3+} and Cr^{3+} ions in $RCrO_3$ with: (a) R^{3+} treated as nonmagnetic ion with $4f$ electrons frozen at the ionic core for the PBE + U and (b) R^{3+} treated as magnetic ion with $4f$ electrons solved explicitly for the SCAN + U.

[35]. Following the experimental evidence that the G-type spin structure is observed for both R^{3+} and Cr^{3+} sublattices from neutron elastic-scattering measurements, the G-AFM spin arrangement is considered for both Cr^{3+} and R^{3+} moments in this work to save computation time [35]. Two typical spin configurations are proposed in the simulations: (i) R^{3+} cations were treated as nonmagnetic with the $4f$ electrons frozen at the ionic core in simulations with PBE + U, and (ii) R^{3+} cations were allowed to order magnetically with the $4f$ electrons treated as valence electrons in simulations with SCAN + U. The two spin configurations for Cr^{3+} and R^{3+} sublattice were initialized in G-AFM order in a 20-atom unit cell as shown in Fig. 1. A full structural relaxation with the R^{3+} and Cr^{3+} magnetic moments initialized was conducted within a self-consistent field calculation of the electronic structure. The resulting ground-state configuration is analyzed focusing on the ground-state band structure, magnetic moments, and structural parameters.

Tables I and II summarize the ground-state magnetic moments of ions in a representative material $GdCrO_3$ in $RCrO_3$, which was optimized by the PBE + U and SCAN + U simulations, respectively. In these tables, the contributions to the total (spin) magnetic moments of s, p, d, and f electrons are listed. It is observed that the major contribution to total magnetic moments is from electrons of d and f shells for Cr^{3+} and Gd^{3+}, respectively. The calculations predict that both Gd^{3+} and Cr^{3+} sublattice moments align antiferromagnetically in a collinear fashion. A zero net total moment of $GdCrO_3$ is observed in the present PBE + U and SCAN + U simulations. Similar results (negligible net total moments of $RCrO_3$) were reported in other rare-earth chromites in SCAN + U simulations, indicating the predominant antiferromagnetic spin configuration in $RCrO_3$ ground state.

TABLE I. Details of the optimized magnetic moments in $GdCrO_3$ calculated by PBE + U. The atomic positions (a_x, b_y, c_z) of listed atoms are as follows: Gd (1): (0.982, 0.065, 0.250), Gd (2): (0.018, 0.935, 0.750), Gd (3): (0.482, 0.435, 0.750), Gd (4): (0.518, 0.565, 0.250), Cr (1): (0.500, 0, 0), Cr (2): (0, 0.500, 0), Cr (3): (0.500, 1.000, 0.500), and Cr (4): (1.000, 0.500, 0.500).

Atom	s (μ_B)	p (μ_B)	d (μ_B)	Total moment (μ_B)
Gd (1)	−0.00	−0.00	0.00	0.00
Gd (2)	0.00	0.00	−0.00	−0.00
Gd (3)	−0.00	−0.00	0.00	0.00
Gd (4)	0.00	0.00	−0.00	−0.00
Cr (1)	−0.02	−0.03	−2.87	−2.93
Cr (2)	0.02	0.03	2.87	2.93
Cr (3)	0.02	0.03	2.87	2.93
Cr (4)	−0.02	−0.03	−2.87	−2.93
Total	0.00	0.00	0.00	0.00

TABLE II. Details of the optimized magnetic moments in $GdCrO_3$ calculated by SCAN + U. The atomic (a_x, b_y, c_z) positions of listed atoms are as follows: Gd (1): (0.982, 0.064, 0.250), Gd (2): (0.018, 0.936, 0.750), Gd (3): (0.482, 0.436, 0.750), Gd (4): (0.518, 0.564, 0.250), Cr (1): (0.500, 0, 0), Cr (2): (0, 0.500, 0), Cr (3): (0.500, 1.000, 0.500), and Cr (4): (1.000, 0.500, 0.500).

Atom	s (μ_B)	p (μ_B)	d (μ_B)	f (μ_B)	Total moment (μ_B)
Gd (1)	−0.01	−0.03	0.10	7.01	7.08
Gd (2)	0.01	0.03	−0.10	−7.01	−7.08
Gd (3)	−0.01	−0.03	0.10	7.01	7.08
Gd (4)	0.01	0.03	−0.10	−7.01	−7.08
Cr (1)	−0.02	−0.03	−2.85	0.00	−2.90
Cr (2)	0.02	0.03	2.85	0.00	2.90
Cr (3)	0.02	0.03	2.85	0.00	2.90
Cr (4)	−0.02	−0.03	−2.85	0.00	−2.90
Total	0.00	0.00	0.00	0.00	0.00

B. Structural properties

The room-temperature XRD patterns of the synthesized $RCrO_3$ (R = Gd, Tb, Dy, Ho, Er, and Tm) samples are presented in Fig. 2, with corresponding Miller indices (hkl) of the characteristic peaks [15,36]. All the peaks can be successfully

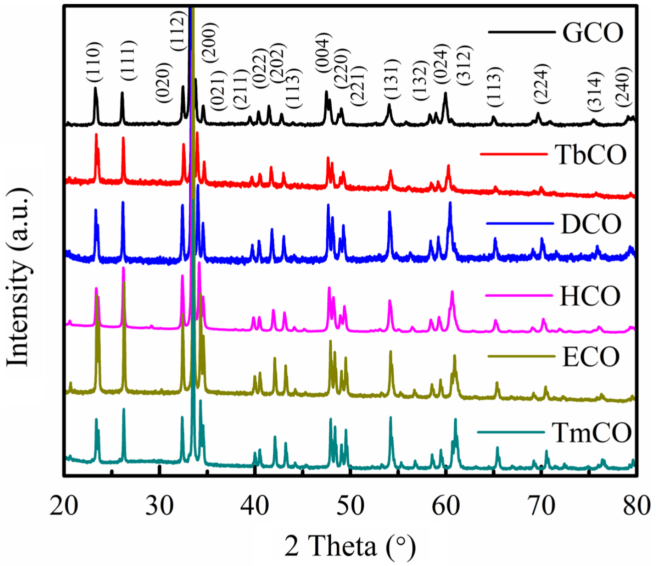

FIG. 2. Room temperature x-ray diffraction patterns of the bulk $RCrO_3$ (RCO).

TABLE III. Experimentally obtained 2-theta (2θ) positions of the (111), (112), (202), (220), and (312) planes in $R\text{CrO}_3$ compounds.

Sample	(111) (°)	(112) (°)	(202) (°)	(220) (°)	(312) (°)
GCO	26.091	33.232	41.446	47.495	59.977
TbCO	26.204	33.373	41.673	47.653	60.278
DCO	26.153	33.363	41.784	47.673	60.460
HCO	26.220	33.428	41.931	47.775	60.674
ECO	26.294	33.525	42.076	47.915	60.904
TmCO	26.254	33.505	42.086	47.935	61.015

indexed in the measured 2-theta (2θ) range, indicating that the samples are of single phase with the space group *Pbnm* and polycrystalline in nature. Table III summarizes the 2θ positions of several representative peaks. The 2θ positions of most crystal planes were found to shift to higher 2θ angles as the rare-earth atom changes from Gd to Tm. In general, changes in the size of the ionic radius of an atom cause the 2θ angle shift and a change in diffraction intensity. The reduction in ionic radius of R^{3+} causes a 2θ angle to shift towards the right (larger angle values), which is in accordance with Bragg's law (θ inversely proportional to the lattice parameter, where the lattice parameter is proportional to the ionic radius). This indicates systematic structural variation in the $R\text{CrO}_3$ series.

The experimentally obtained XRD scans of all samples were fitted by using Rietveld refinements via FULLPROF SUITE software assuming an orthorhombically distorted perovskite structure (space group *Pbnm*) and four formula units per unit cell. Useful structural information was extracted from the refinements and the obtained lattice parameters, bond angles, and unit-cell volumes are summarized in Table IV. The lattice parameters (a and c) and unit-cell volume (V) were found to decrease with the decreasing ionic radii of R^{3+} (from Gd, Tb, Dy, Ho, Er, to Tm). The largest and smallest values of bond angles are observed in GCO and TmCO, respectively. In $R\text{CrO}_3$ with orthorhombically distorted structure, the decreasing values of the out-of-plane Cr–O_1–Cr and in-plane Cr–O_2–Cr bond angles (from an ideal 180° of $AB\text{O}_3$ cubic perovskites structure) that corresponds to the tilting of CrO_6 octahedral, leads to increasing distortion in the structure [37]. In the present work, the Cr–O_1–Cr and Cr–O_2–Cr bond angles were found to decrease with decreasing atomic number of rare earths, which is consistent with the decreasing size of rare-earth cations [15].

TABLE V. Structural parameters obtained from the DFT (PBE + U) simulations.

Sample	a (Å)	b (Å)	c (Å)	V (Å^3)	Cr–O_1–Cr (°)	Cr–O_2–Cr (°)
GCO	5.340	5.614	7.679	230.246	145.60	146.66
TbCO	5.317	5.609	7.657	228.362	144.49	145.83
DCO	5.297	5.600	7.637	226.541	143.45	145.10
HCO	5.277	5.592	7.619	224.809	142.48	144.43
ECO	5.258	5.583	7.602	223.177	141.66	143.84
TmCO	5.237	5.569	7.582	221.147	140.59	143.12

The relaxed lattice parameters were also calculated using DFT calculations. Table V lists lattice parameters obtained using the initial spin configuration presented in Fig. 1(a) and PBE + U simulation, while Table VI lists those using the spin configuration in Fig. 1(b) and SCAN + U simulation. Figure 3 displays the experimental and computed parameters (Table V and Table VI) that indicate that the computed lattice parameters and unit-cell volume depict a trend that is consistent with those obtained experimentally. The Cr–O_1–Cr bond angle is found to be decreasing with reducing ionic radii of rare earth using both PBE + U and SCAN + U simulations. It is evident from Fig. 3 that the SCAN + U predicted lattice parameters are in better agreement with the experimental results compared to the PBE + U simulation. This indicates that the meta-GGA functional facilitates comparatively better calculation of the structural properties of $R\text{CrO}_3$ perovskites. This observation agrees with previous study in which the SCAN meta-GGA was shown to be superior to the PBE GGA for predicting the geometries and energies of diversely bonded materials (including metallic, ionic, hydrogen, covalent, and van der Waals bonds) [38].

The $R\text{CrO}_3$ compounds with *Pbnm* space group contain four formula units per Bravais unit cell. According to the space group, among 60 irreducible representation for vibration modes of atoms at four different Wyckoff sites, only 24 phonon modes ($7A_g + 7B_{1g} + 5B_{2g} + 5B_{3g}$) were reported to be Raman active [39]. Several characteristic Raman modes out of those 24 were observed in the Raman spectra of the present samples as shown in Fig. 4. In these, several modes merged to form a broad peak for some $R\text{CrO}_3$ samples [40]. The assignment of phonon modes to the chromite spectra was carried out according to the works by Weber *et al.* and Camara *et al.* [40,41]. The Raman modes A_g($\sim$140 cm^{-1}) and B_{2g}($\sim$160 cm^{-1}) are induced by displacements of the R-site

TABLE IV. Ionic radii (r) of rare-earth ions $R\text{CrO}_3$ (RCO) and structural parameters of various RCO compounds obtained by Rietveld refinement of the experimentally obtained XRD patterns: lattice parameters: a, b, c; unit-cell volume: V; out-of-plane bond angle Cr–O_1–Cr, and in-plane bond angle Cr-O_2-Cr.

Sample	r (Å)	a (Å)	b (Å)	c (Å)	V (Å^3)	Cr–O_1–Cr (°)	Cr–O_2–Cr (°)
GCO	1.107	5.319	5.527	7.614	223.839	151.4	149.7
TbCO	1.095	5.298	5.523	7.584	221.870	146.6	147.4
DCO	1.083	5.270	5.526	7.562	220.193	146.5	150.5
HCO	1.072	5.252	5.529	7.550	219.202	145.9	148.4
ECO	1.062	5.229	5.521	7.526	217.275	144.8	144.6
TmCO	1.052	5.213	5.512	7.508	215.737	147.0	143.6

TABLE VI. Structural parameters obtained from the DFT (SCAN + U) simulations.

Sample	a (Å)	b (Å)	c (Å)	V (Å^3)	Cr–O$_1$–Cr (°)	Cr–O$_2$–Cr (°)
GCO	5.320	5.577	7.637	226.565	146.42	147.26
TbCO	5.284	5.555	7.592	222.857	144.24	145.69
DCO	5.262	5.525	7.570	220.074	142.92	144.44
HCO	5.224	5.517	7.538	217.223	141.56	143.47
ECO	5.241	5.535	7.548	218.939	142.08	143.95
TmCO	5.199	5.506	7.514	215.081	140.27	142.61

ions since the heaviest atom of the structure is anticipated to vibrate at the low wave-number region [40]. Bands in the midspectral region (200–400 cm^{-1}), such as A_g(∼260 cm^{-1}), A_g(∼330 cm^{-1}), and A_g(∼400 cm^{-1}) are very sensitive to the changes in the orthorhombic distortion. Two modes A_g(3) and A_g(5) have been identified as octahedral rotation soft modes, as Raman shifts scale linearly with the tilt angle of the CrO$_6$ octahedra [40]. Both A_g(3) and A_g(5) are found to increase with the decreasing of the ionic radii of rare earth, indicating a larger tilt angle [= {180-(Cr-O$_1$-Cr)}/2] for RCrO$_3$ with smaller ionic radii. This observation agrees with the results predicted by the DFT-predicted bond angle in Fig. 3(iii). The experimentally obtained Raman shift of some modes for all samples are summarized in Table VII and for some representative modes are plotted in Fig. 5, which depicts that Raman modes shifted to lower wave numbers with the increasing ionic radii.

C. Optic and electronic properties

The UV–Vis diffuse reflectance spectroscopy was used to probe the electronic behaviors present in the RCrO$_3$, such as electronic transitions of the different orbitals of a solid [42]. The reflectance spectra obtained from the present samples are plotted in Fig. 6(a). To determine the band gap, the measured reflectance (R') needs to be converted to its corresponding absorption ($F_{R'}$) according to the Kubelka-Munk

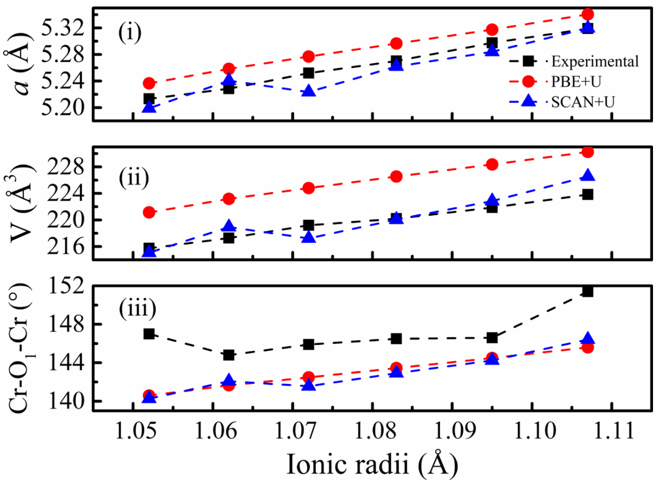

FIG. 3. Comparison of (i) lattice parameter a, (ii) unit-cell volume (V), and (iii) out-of-plane bond angle Cr–O$_1$–Cr obtained from DFT and Rietveld refinement of the experimental XRD data.

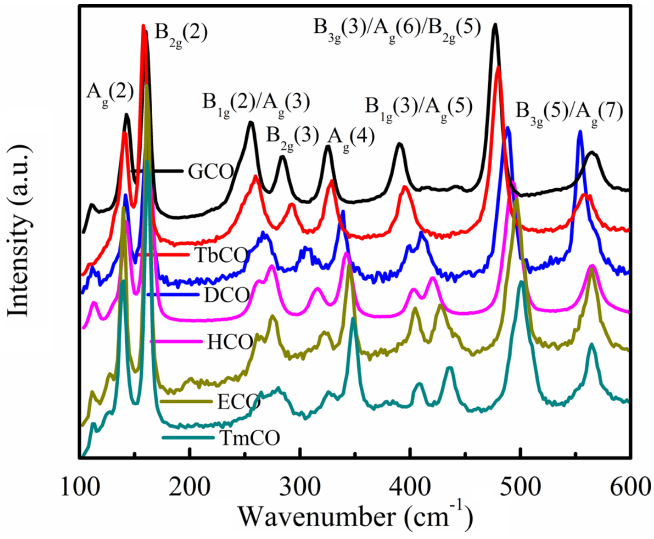

FIG. 4. Room-temperature Raman spectra of rare-earth chromites.

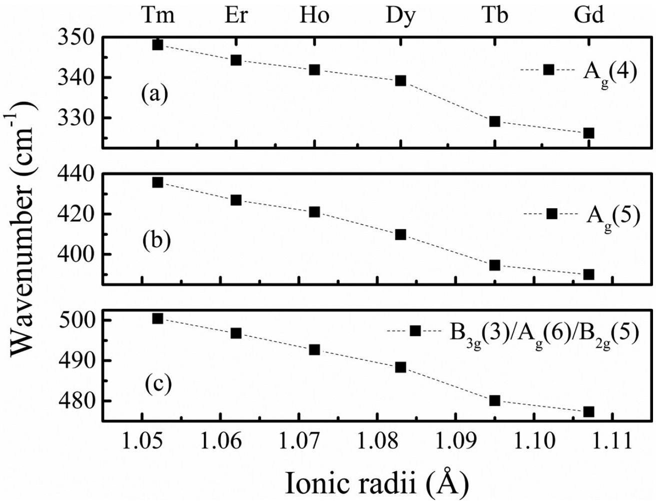

FIG. 5. Evolution of the room-temperature Raman modes′ position with ionic radii of R^{3+} in RCrO$_3$.

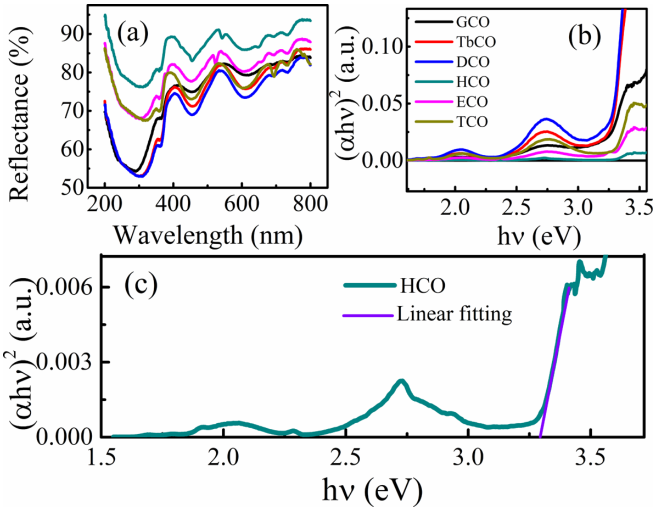

FIG. 6. (a) UV-Vis diffuse reflectance spectra and (b) optical absorption plots $(\alpha h\nu)^2$ of rare-earth chromites. (c) Optical absorption edge of HoCrO$_3$ with linear fit.

TABLE VII. Experimentally observed Raman shifts of different modes.

Sample	$B_{2g}(2)$ (cm^{-1})	$A_g(3)$ (cm^{-1})	$A_g(4)$ (cm^{-1})	$A_g(5)$ (cm^{-1})	$B_{3g}(3)/A_g(6)/B_{2g}(5)$ (cm^{-1})
GCO	160.243	254.964	326.219	390.039	477.263
TbCO	157.887	259.610	329.099	394.616	480.094
DCO	162.914	266.324	339.219	409.809	488.344
HCO	162.137	274.266	341.914	421.049	492.693
ECO	161.086	274.968	344.338	426.876	496.775
TmCO	161.354	280.455	348.055	435.690	500.429

function [42]:

$$F_{R'} = \frac{(1-R')^2}{2R'}. \tag{1}$$

In order to calculate the band gap, Tauc's equation is employed as below [43]:

$$\alpha h\nu = B(h\nu - E_g)^n. \tag{2}$$

Here, α is the optical absorption coefficient, h is the Planck constant, ν is the photon's frequency, B is a characteristic parameter, E_g is the energy band gap, and n is the 1/2 for a direct allowed transition. Here, $F_{\mathrm{R}'}$ has been put into Eq. (2) as α [43]. Based on Eq. (2), the plot of $(\alpha h\nu)^2$ versus energy $h\nu$ is presented in Fig. 6(b). For the determination of optical band gap, a representative case of HCO is demonstrated separately in Fig. 6(c). The region with a linear increase in $(\alpha h\nu)^2$ with increasing energy in Tauc plot is characteristic of the semiconductor materials and can be linearly fitted. The estimation of the band gap can thus be obtained by the extrapolation of the linear fit and the point of intersection on the x axis and is shown as a purple solid line in Fig. 6(c). The experimental optical band gaps thus obtained for all $R\mathrm{CrO}_3$ are tabulated in Table VIII. It can be noticed that the band gap for GCO, TbCO, DCO, HCO, ECO, and TmCO is 3.21, 3.27, 3.28, 3.29, 3.28, and 3.29 eV, respectively. These observed values of band gap are close to some of the reported band gaps of $R\mathrm{CrO}_3$ [17]. This wide band gap (~3.3 eV) of the present $R\mathrm{CrO}_3$ can be possibly attributed to the charge-transfer gap of O^{2-} $2p$-$\mathrm{Cr}^{3+}3d(t_{2g})$ [17,44].

The first-principles calculations were also carried out to understand the electronic and optical properties of $R\mathrm{CrO}_3$. We have calculated the band gaps for the RCrO_3 using the *spin-polarized* PBE + U and SCAN + U with VASP. Figure 7 presents the band structures of $R\mathrm{CrO}_3$ materials calculated by PBE + U (for spin up [Fig. 7(a)] and spin down [Fig. 7(b)]), where the top of the valence band is set to be zero (Fermi level, E_F) for convenience. It can be seen that all the members of $R\mathrm{CrO}_3$ studied here exhibit very similar band structure. It is also observed that $R\mathrm{CrO}_3$ is an indirect-gap semiconductor since the highest occupied orbitals and the minimum of the lowest unoccupied orbitals occur at the point S and Γ, respectively. The density of states (DOS) of all $R\mathrm{CrO}_3$ materials is plotted as a function of energy in Fig. 8(a) that exhibits similar energy gap for all with a value around 2.6 eV (also listed in Table VIII). This band-gap value for $R\mathrm{CrO}_3$ is lower than the experimentally obtained values mentioned above. This is expected as the GGA-PBE always underestimates the electronic band gap [45]. In the vicinity of E_F (−3 eV – 0 eV) of the valence band of GCO, the majority of the DOS arises from the d states of Cr and p states of O [29]. The bottom of the conduction band is composed of O $2p$ and Cr $3d$ orbitals, but is mainly dominated by Cr $3d$ orbitals. Therefore, the observed optical transition originates from O $2p$ orbitals of valence band to Cr $3d$ orbitals of conduction band.

Here, we have proposed the SCAN functional to calculate the band structure of $R\mathrm{CrO}_3$, as SCAN is proved to be better than the PBE version of the GGA exchange-correlation functional in reproducing accurate and correct ground-state structures of several other compounds [46]. However, SCAN functional also requires a Hubbard U correction to reproduce the ground-state lattice parameters, magnetic moments, and electronic properties of several materials such as Ce-, Mn-, and Fe-based oxide [46]. To explore whether SCAN + U scheme can give a reasonably accurate description of the electronic structure of the $R\mathrm{CrO}_3$ material, the DFT calculations for two representative $R\mathrm{CrO}_3$ (GdCrO_3 and DyCrO_3) were performed with a series of U values assigned to $4f$ and $3d$ orbitals. Figure 9 displays the variation of total and projected DOS of GdCrO_3 with the Hubbard U ranging from 0 to 3 eV and 0 to 4.6 eV for Cr and Gd, respectively. Firstly, without accounting for the on-site Coulomb repulsion among the $3d$ and $4f$ electrons ($U = 0$ eV), a band gap of 2.60 eV is observed and the $4f$ states are delocalized within the O $2p$ band. By introducing the on-site Hubbard repulsion upon $3d$ states ($U = 3$ eV for Cr), the band gap is found to increase and the $4f$ states still reside within the O $2p$ band. Intriguingly, when the on-site repulsion among $4f$ electrons is taken into consideration, the separation of $4f$ states gradually increases with the increasing U value of Gd (due to stronger orbital repulsion). However, the band gap does not increase with the increasing Hubbard-U value on $4f$, indicating that the band

TABLE VIII. Band gap of RCrO_3 obtained from the Tauc plot (experimental) and DFT (PBE + U, SCAN + U) calculations.

Sample	Experimental (eV)	DFT (PBE + U) (eV)	DFT (SCAN + U) (eV)
GCO	3.21	2.61	3.46
TbCO	3.27	2.62	2.92
DCO	3.28	2.63	3.43
HCO	3.29	2.65	3.53
ECO	3.28	2.66	3.44
TmCO	3.29	2.66	3.52

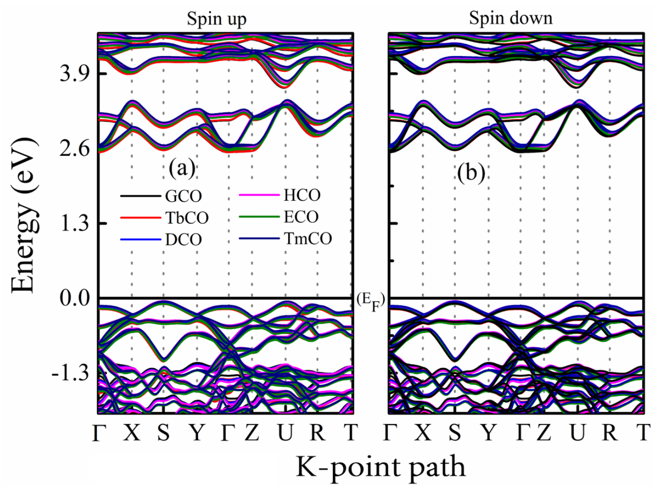

FIG. 7. Band structure of $R\mathrm{CrO}_3$ calculated by PBE + U simulation: (a) up spins and (b) down spins. The top of valence band is set to be zero (Fermi level, E_F).

gap is principally determined by the position of conduction $3d$ and valence $2p$ states in GdCrO_3. Finally, when the U value for Gd increases to the suggested value of 4.6 eV in Ref. [34], a gap opens between the Gd $4f$ and O $2p$ bands and the $4f$ bands locate approximately 5 eV below the E_F. In the case of DyCrO_3, SCAN alone tends to underestimate the band gap and place f states close to the E_F as shown in Fig. 10(a). With the introduction of a U correction of 5 eV for Dy, a gap opens up between the Dy $4f$ states and O $2p$ states as depicted in Fig. 10(b). The variation of the R $4f$ electronic structures of the two materials under different U values agrees with the previous viewpoint that proper Hubbard-U values are required to place f states in positions like those produced by the hybrid functional [34]. Therefore, the U values suggested by Topsakal *et al.* are employed as the Hubbard-U parameter for $4f$ orbitals of rare-earth ions in the subsequent calculations [34].

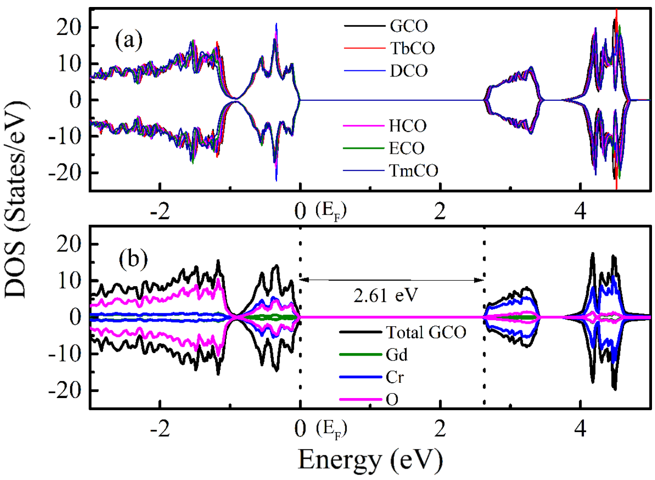

FIG. 8. (a) Calculated total density of states for $R\mathrm{CrO}_3$ by the PBE + U simulation. (b) Calculated total and atom-projected DOS of GdCrO_3 by the PBE + U simulation. The top of valence band is set to be zero (Fermi level, E_F).

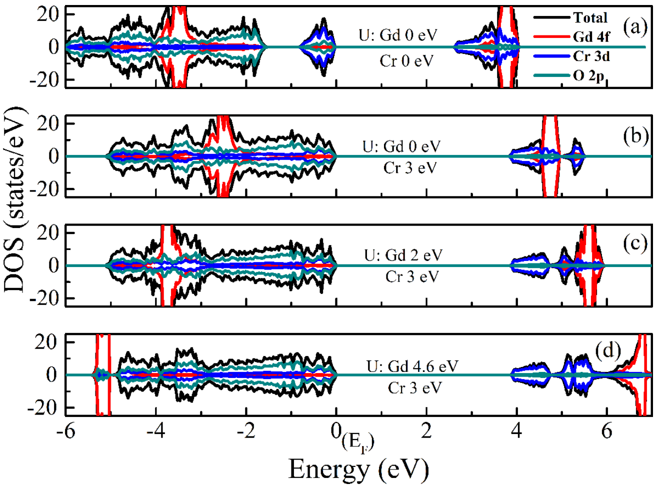

FIG. 9. Calculated total and projected DOS of GdCrO_3 by the SCAN + U simulation with a series of U trials. The Hubbard-U corrections for Gd and Cr are (a) 0 and 0 eV, (b) 0 and 3 eV, (c) 2 and 3e V, and (d) 4.6 and 3 eV, respectively. This figure shows how the band gap is affected by the chosen U values and the resulting orbital repulsions.

The band structures of RCrO_3 and their corresponding total and projected DOS are calculated within the SCAN + U scheme and plotted in Figs. 11 and 12, respectively. The band structure shown in Fig. 11 also confirms that $R\mathrm{CrO}_3$ materials studied here are indirect band-gap semiconductors, for the valence-band maximum at S-point and the conduction-band minimum at Γ-point. Figure 12 shows the density of spin-up and spin-down states of $R\mathrm{CrO}_3$ both behaving as semiconductor, consistent with previous band-structure calculations in Fig. 11. The contribution from R $4f$, Cr $3d$, and O $2p$ states to the total DOS have been explicitly plotted and used to determine the type of band gap. The top of the valence band shows an O $2p$ character, while the bottom of the conduction band

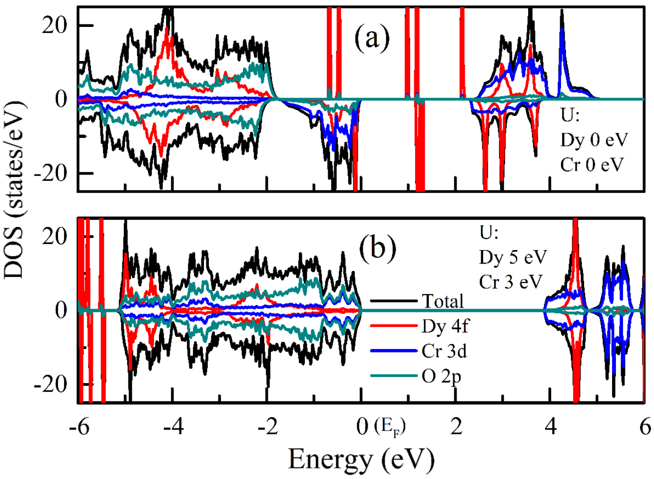

FIG. 10. Calculated total and projected DOS of DyCrO_3 by the SCAN + U simulation with Hubbard-U corrections for Dy and Cr as (a) 0 and 0 eV and (b) 5 and 3 eV, respectively. This figure also shows how the U parameter affects the orbital repulsions and band gaps.

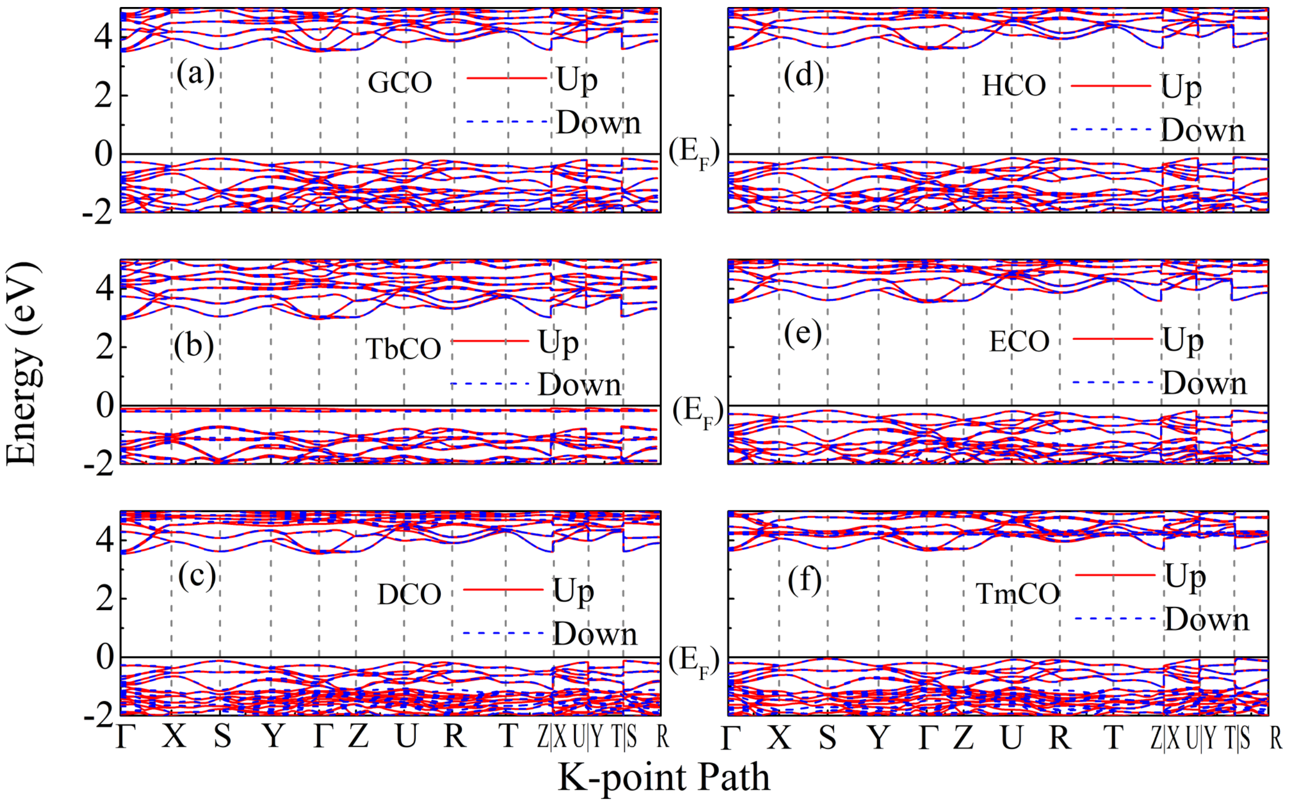

FIG. 11. Calculated band structure by SCAN with Hubbard-U correction: (a) $GdCrO_3$, (b) $TbCrO_3$, (c) $DyCrO_3$, (d) $HoCrO_3$, (e) $ErCrO_3$, and (f) $TmCrO_3$. The top of valence band is set to be zero (Fermi level, E_F).

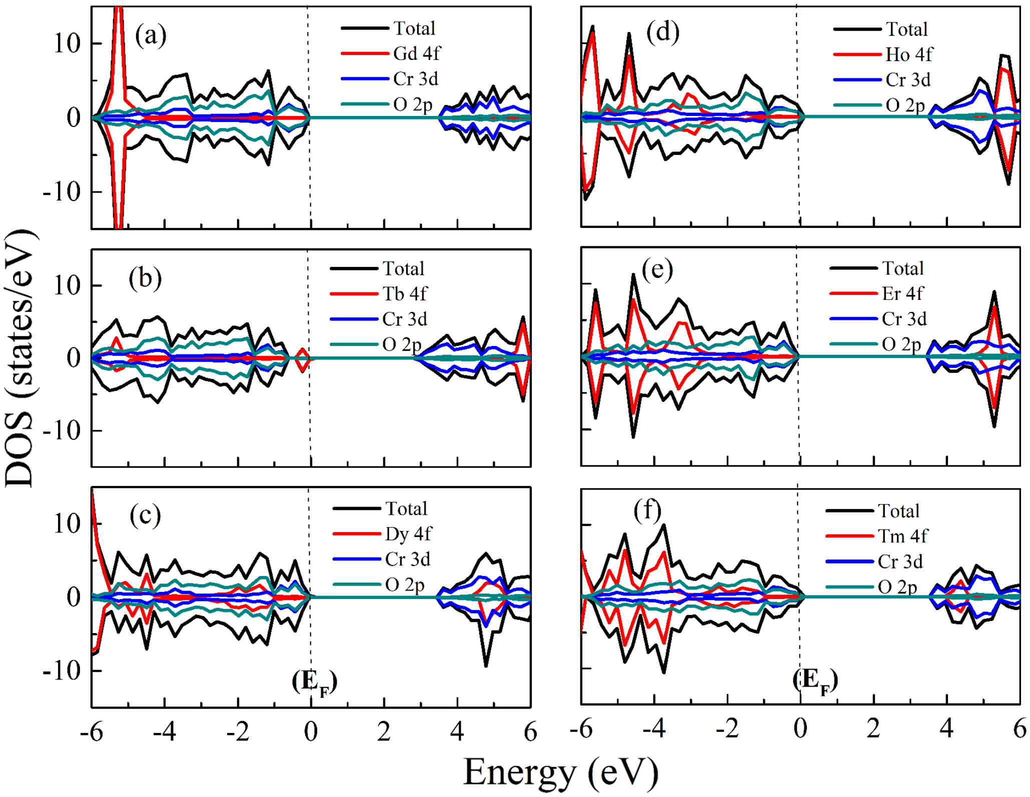

FIG. 12. Calculated and atom projected DOS by SCAN + U simulation: (a) $GdCrO_3$, (b) $TbCrO_3$, (c) $DyCrO_3$, (d) $HoCrO_3$, (e) $ErCrO_3$, and (f) $TmCrO_3$. The top of valence band is set to be zero (Fermi level, E_F).

has a Cr $3d$ character [47]. The contribution from the O $2p$ state dominates in the energy range below Fermi level, while the Cr $3d$ state contribution is more above Fermi level in the conduction band. The contribution from R $4f$ crossing the E_F is negligible when compared to the contribution from Cr $3d$ and O $2p$ states. According to the charge-transfer (CT) energy required to move an electron from the anion valence band to the d orbitals at the transition-metal site, $R\mathrm{CrO}_3$ can be classified as CT semiconductors with a p–d-type gap between the O^{2-} $2p$ filled band and the Cr^{3+} $3d$ upper Hubbard band [48]. The band gaps of GCO, TbCO, DCO, HCO, ECO, and TmCO are estimated to be 3.46, 2.92, 3.43, 3.53, 3.44, and 3.52 eV, respectively from Fig. 12, as listed in Table VIII. Obviously, the present energy gap is slightly wider than the experimentally obtained energy-gap value of ∼3.2 eV, and also wider than another calculation result of ∼2.7 eV by PBE + U. The calculated results here clearly indicate that the SCAN + U could reproduce the Cr $3d$ and O $2p$ bands crossing the Fermi level more accurately than that by PBE + U.

IV. CONCLUSIONS

A comprehensive study in terms of structural, optical, and electronic properties of $R\mathrm{CrO}_3$ (for $R =$ Gd, Tb, Dy, Ho, Er, and Tm) has been carried out on all the samples both experimentally and theoretically by first-principles density-functional theory. Band gap and structural distortions of $R\mathrm{CrO}_3$ in terms of Cr–O–Cr bond angles, unit-cell volume, and lattice parameters have been experimentally determined from the UV-Vis spectra and Rietveld refinement of the x-ray diffraction scans, respectively. The lattice parameters a and c were found to consistently reduce with decreasing ionic radii of the R^{3+} ion. Raman modes, such as $A_g(3)$ and $A_g(5)$, were found to shift to lower wave numbers with increasing ionic radii of R^{3+}, indicating a consistent structural distortion associated with octahedral rotation. The optical band gap of $R\mathrm{CrO}_3$ revealed by UV-Vis spectra was ∼3.3 eV. We also evaluated the performance of generalized gradient approximation (PBE) and meta-GGA (SCAN) functional with Hubbard-U correction for predicting the structural and electronic properties in these perovskite-type $R\mathrm{CrO}_3$. The severe crystal distortion with smaller R^{3+} ionic radius was also revealed by both PBE + U and SCAN + U DFT simulations, which agrees with the results obtained from XRD and Raman spectra. It was found that the SCAN + U framework could reproduce a more accurate ground-state crystal structure than that predicted by PBE + U. The band gap of $R\mathrm{CrO}_3$ predicted by SCAN + U simulation (∼3.4 eV) is closer to the band gap (∼3.3 eV) determined experimentally, while the band gap calculated by PBE + U (∼2.6 eV) differs from experimental values. Thus, in this study SCAN + U is shown to be superior to PBE + U in predicting both the structural properties and band structure of $R\mathrm{CrO}_3$.

ACKNOWLEDGMENTS

M.J. acknowledges National Science Foundation (CBET 2233149), UConn Institute of Materials Science - Interdisciplinary Multi-Investigator Materials Program as well as UConn College of Liberal Arts and Sciences for financial support for this research. The VASP calculations were performed using the *ab initio* total-energy and molecular-dynamics program developed at the Fakultät für Physik of the Universität Wien [31,32], under a software license agreement between GWF's research group at UConn and the Universität Wien. We also acknowledge the computing resources provided by the Center for Functional Nanomaterials, which is a U.S. Department of Energy (DOE) Office of Science Facility, at Brookhaven National Laboratory under Contract No. DE-SC0012704. S.L.S. thanks the U.S. DOE, Office of Basic Energy Sciences, under Grant No. DE-FG02-86ER13622 for support of this research.

[1] L. Yin, J. Yang, P. Tong, X. Luo, C. Park, K. Shin, W. Song, J. Dai, K. Kim, and X. Zhu, Role of rare earth ions in the magnetic, magnetocaloric and magnetoelectric properties of RCrO_3 (R = Dy, Nd, Tb, Er) crystals, J. Mater. Chem. C. **4**, 11198 (2016).

[2] H. Yamamoto, S. Okamoto, and H. Kobayashi, Luminescence of rare-earth ions in perovskite-type oxides: From basic research to applications, J. Lumin. **100**, 325 (2002).

[3] M. K. Warshi, V. Mishra, A. Sagdeo, V. Mishra, R. Kumar, and P. Sagdeo, Structural, optical and electronic properties of RFeO_3, Ceram. Int. **44**, 8344 (2018).

[4] Y. Ye, A. Cui, M. Bian, K. Jiang, L. Zhu, J. Zhang, L. Shang, Y. Li, Z. Hu, and J. Chu, Temperature and pressure manipulation of magnetic ordering and phonon dynamics with phase transition in multiferroic GdFeO 3: Evidence from Raman scattering, Phys. Rev. B **102**, 024103 (2020).

[5] A. Akbashev, A. Semisalova, N. Perov, and A. Kaul, Weak ferromagnetism in hexagonal orthoferrites RFeO3 (R = Lu, Er-Tb), Appl. Phys. Lett. **99**, 122502 (2011).

[6] Y. Tokura and Y. Tomioka, Colossal magnetoresistive manganites, J. Magn. Magn. Mater. **200**, 1 (1999).

[7] D. V. Efremov, J. Van Den Brink, and D. I. Khomskii, Bond-versus site-centred ordering and possible ferroelectricity in manganites, Nat. Mater. **3**, 853 (2004).

[8] T. Goto, T. Kimura, G. Lawes, A. Ramirez, and Y. Tokura, Ferroelectricity and Giant Magnetocapacitance in Perovskite Rare-Earth Manganites, Phys. Rev. Lett. **92**, 257201 (2004).

[9] G. Giovannetti, S. Kumar, D. Khomskii, S. Picozzi, and J. van den Brink, Multiferroicity in Rare-Earth Nickelates R NiO_3, Phys. Rev. Lett. **103**, 156401 (2009).

[10] S. Catalano, M. Gibert, J. Fowlie, J. Iniguez, J.-M. Triscone, and J. Kreisel, Rare-earth nickelates RNiO_3: Thin films and heterostructures, Rep. Prog. Phys. **81**, 046501 (2018).

[11] J. Varignon, M. N. Grisolia, J. Íñiguez, A. Barthélémy, and M. Bibes, Complete phase diagram of rare-earth nickelates from first-principles, npj Quantum Mater. **2**, 1 (2017).

[12] J. R. Sahu, C. R. Serrao, N. Ray, U. V. Waghmare, and C. Rao, Rare earth chromites: A new family of multiferroics, J. Mater. Chem. **17**, 42 (2007).

[13] R. Saha, A. Sundaresan, and C. Rao, Novel features of multiferroic and magnetoelectric ferrites and chromites exhibiting magnetically driven ferroelectricity, Mater. Horiz. **1**, 20 (2014).

[14] S. K. Joshi and R. A. Mashelkar, *Solid State Chemistry: Selected Papers of C.N.R. Rao* (World Scientific Publishing Co., Singapore, 1995), Vol. 4, p. 365.

[15] J. Prado-Gonjal, R. Schmidt, J.-J. Romero, D. Ávila, U. Amador, and E. Morán, Microwave-assisted synthesis, microstructure, and physical properties of rare-earth chromites, Inorg. Chem. **52**, 313 (2013).

[16] K. D. Singh, F. Singh, R. Choudhary, and R. Kumar, Consequences of R^{3+} cationic radii on the dielectric and magnetic behavior of RCrO$_3$ perovskites, Appl. Phys. A **126**, 1 (2020).

[17] K. D. Singh, R. Pandit, and R. Kumar, Effect of rare earth ions on structural and optical properties of specific perovskite orthochromates; RCrO$_3$ (R = La, Nd, Eu, Gd, Dy, and Y), Solid State Sci. **85**, 70 (2018).

[18] G. Oliveira, A. Pires, P. Machado, A. Pereira, J. Araújo, and A. Lopes, Effect of chemical pressure on the magnetocaloric effect of perovskite-like RCrO$_3$ (R-Yb, Er, Sm and Y), J. Alloys Compd. **797**, 269 (2019).

[19] S. Mahana, U. Manju, P. Nandi, E. Welter, K. Priolkar, and D. Topwal, Role of local structural distortion in driving ferroelectricity in GdCrO$_3$, Phys. Rev. B **97**, 224107 (2018).

[20] H. J. Zhao, L. Bellaiche, X. M. Chen, and J. Íñiguez, Improper electric polarization in simple perovskite oxides with two magnetic sublattices, Nat. Commun. **8**, 14025 (2017).

[21] J. H. Yang, D. A. Kitchaev, and G. Ceder, Rationalizing accurate structure prediction in the meta-GGA SCAN functional, Phys. Rev. B **100**, 035132 (2019).

[22] R. Godby, M. Schlüter, and L. Sham, Accurate Exchange-Correlation Potential for Silicon and Its Discontinuity on Addition of an Electron, Phys. Rev. Lett. **56**, 2415 (1986).

[23] K. Terakura, T. Oguchi, A. Williams, and J. Kübler, Band theory of insulating transition-metal monoxides: Band-structure calculations, Phys. Rev. B **30**, 4734 (1984).

[24] R. Albers, N. E. Christensen, and A. Svane, Hubbard-U band-structure methods, J. Phys.: Condens. Matter. **21**, 343201 (2009).

[25] B. Himmetoglu, A. Floris, S. De Gironcoli, and M. Cococcioni, Hubbard-corrected DFT energy functionals: The LDA + U description of correlated systems, Int. J. Quantum Chem. **114**, 14 (2014).

[26] M. Staruch, V. Sharma, C. dela Cruz, R. Ramprasad, and M. Jain, Magnetic ordering in TbMn0. 5Cr0. 5O3 studied by neutron diffraction and first-principles calculations, J. Appl. Phys. **116**, 033919 (2014).

[27] S. Terkhi, S. Bentata, Z. Aziz, T. Lantri, and B. Abbar, First principle calculations of structural, electronic and magnetic properties of cubic GdCrO$_3$ perovskite, Indian J. Phys. **92**, 847 (2018).

[28] S. Terkhi, R. Bentata, F. Bendahma, T. Lantri, S. Bentata, Z. Aziz, and B. Abbar, Half-metallic ferromagnetic behavior of cubic lanthanide based on perovskite-type oxide NdCrO$_3$: First-principles calculations, Indian J. Phys. **95**, 833 (2021).

[29] S. Yin, V. Sharma, A. McDannald, F. A. Reboredo, and M. Jain, Magnetic and magnetocaloric properties of iron substituted holmium chromite and dysprosium chromite, RSC Adv. **6**, 9475 (2016).

[30] K. P. Ong, P. Blaha, and P. Wu, Origin of the light green color and electronic ground state of LaCr O$_3$, Phys. Rev. B **77**, 073102 (2008).

[31] G. Kresse and J. Furthmüller, Efficient iterative schemes for ab initio total-energy calculations using a plane-wave basis set, Phys. Rev. B **54**, 11169 (1996).

[32] G. Kresse and D. Joubert, From ultrasoft pseudopotentials to the projector augmented-wave method, Phys. Rev. B **59**, 1758 (1999).

[33] I.-G. Buda, C. Lane, B. Barbiellini, A. Ruzsinszky, J. Sun, and A. Bansil, Characterization of thin film materials using SCAN meta-GGA, an accurate nonempirical density functional, Sci. Rep. **7**, 1 (2017).

[34] M. Topsakal and R. Wentzcovitch, Accurate projected augmented wave (PAW) datasets for rare-earth elements (*RE* = La–Lu), Comput. Mater. Sci. **95**, 263 (2014).

[35] N. Shamir, H. Shaked, and S. Shtrikman, Magnetic structure of some rare-earth orthochromites, Phys. Rev. B **24**, 6642 (1981).

[36] S. Yuling, J. Zhang, F. Zhenjie, L. Zijiong, S. Yan, and C. Shixun, Magnetic properties of rare earth HoCrO$_3$ chromites, J. Rare Earths **29**, 1060 (2011).

[37] S. Wang, X. Wu, T. Wang, J. Zhang, C. Zhang, L. Yuan, X. Cui, and D. Lu, Mild hydrothermal crystallization of heavy rare-earth chromite RECrO$_3$ (RE = Er, Tm, Yb, Lu) perovskites and magnetic properties, Inorg. Chem. **58**, 2315 (2019).

[38] Y. Zhang, J. Sun, J. P. Perdew, and X. Wu, Comparative first-principles studies of prototypical ferroelectric materials by LDA, GGA, and SCAN meta-GGA, Phys. Rev. B **96**, 035143 (2017).

[39] Y. Jana, J. Saha, and S. Nandi, Assignment of optical phonons at the zone center of distorted orthorhombic RCrO$_3$ (R = La, Pr, Nd, Sm, Eu) perovskites using force-field lattice dynamics model, Vib. Spectrosc. **109**, 103086 (2020).

[40] M. Weber, J. Kreisel, P. Thomas, M. Newton, K. Sardar, and R. Walton, Phonon Raman scattering of RCrO$_3$ perovskites (R = Y, La, Pr, Sm, Gd, Dy, Ho, Yb, Lu), Phys. Rev. B **85**, 054303 (2012).

[41] N. R. Camara, V. Ta Phuoc, I. Monot-Laffez, and M. Zaghrioui, Polarized Raman scattering on single crystals of rare earth orthochromite RCrO$_3$ (R = La, Pr, Nd, and Sm), J. Raman Spectrosc. **48**, 1839 (2017).

[42] R. López and R. Gómez, Band-gap energy estimation from diffuse reflectance measurements on sol–gel and commercial TiO$_2$: A comparative study, J. Solgel Sci. Technol. **61**, 1 (2012).

[43] P. Makuła, M. Pacia, and W. Macyk, How to correctly determine the band gap energy of modified semiconductor photocatalysts based on UV–Vis spectra, J. Phys. Chem. Lett. **9**, 6814 (2018).

[44] V. R. Mannepalli, M. S. Mohan, and R. Ranjith, Tailoring the bandgap and magnetic properties by bismuth substitution in neodymium chromite, Bull. Mater. Sci. **40**, 1503 (2017).

[45] H. Shaili, E. mehdi Salmani, M. Beraich, R. Essajai, W. Battal, M. Ouafi, A. Elhat, M. Rouchdi, M. Taibi, H. Ez-Zahraouy *et al.*, Enhanced properties of the chemically prepared

Gd-doped $SrSnO_3$ thin films: Experimental and DFT study, Opt. Mater. **107**, 110136 (2020).

[46] O. Y. Long, G. S. Gautam, and E. A. Carter, Evaluating optimal U for 3 d transition-metal oxides within the SCAN + U framework, Phys. Rev. Mater. **4**, 045401 (2020).

[47] R. Hossain, A. Billah, M. Ishizaki, S. Kubota, F. Hirose, and B. Ahmmad, Oxygen vacancy mediated room-temperature ferromagnetism and bandgap narrowing in $DyFe_{0.5}Cr_{0.5}O_3$ nanoparticles, Dalton Trans. **50**, 9519 (2021).

[48] Y. Li, Y.-S. Zheng, Y.-A. Zhu, Z.-J. Sui, X.-G. Zhou, D. Chen, and W.-K. Yuan, BEEF-vdW + U method applied to perovskites: Thermodynamic, structural, electronic, and magnetic properties, J. Phys.: Condens. Matter. **31**, 145901 (2019).